Chemical Engineering Journal 545 (2026) 179304

Contents lists available at ScienceDirect

Chemical Engineering Journal

journal homepage: www.elsevier.com/locate/cej

Triple-phase Interface-induced triboelectric-liquid capacitance coupling: Unlocking high power direct-current triboelectric nanogenerators

Xin-Long Xiao [a,b,1], Jiang-Tao Guo [b,1], Sheng-Jie Lin [a,b], Wen Yang [b], Yun-Bo Zhang [b], Yong Zhang [c], Pei-Zhi Yang [a,b,*]

[a] Yunnan Normal University, School of Energy and Environment Science, Southwest United Graduate School, No. 298, Yieryi Street, Kunming, Yunnan, 650092, China
[b] Yunnan Normal University, School of Energy and Environment Science, No.768, Juxian Street, Chenggong District, Kunming, Yunnan 650500, China
[c] Department of Electrical and Computer Engineering and Center for Optoelectronics, University of North Carolina at Charlotte, Charlotte, NC, 28223, USA

ARTICLE INFO

Keywords:
Triple-phase interface
Triboelectric-liquid capacitance coupling
Direct-current triboelectric nanogenerator
Flexible micropower source
Electrostatic shielding suppression

ABSTRACT

Traditional solid-solid triboelectric nanogenerators (TENGs) are hindered by mechanical wear and inherent alternating-current generation, while existing solid-liquid TENGs suffer from electrostatic shielding and limited power density. Herein, we report a flexible, DC-output liquid-contact TENG (LC-TENG) constructed using a porous polytetrafluoroethylene/carbon black heterostructure featuring solid-liquid-air triple-phase interfaces. This structural design effectively suppresses electrostatic shielding and converts triboelectric effect into an asymmetric charge pump, enabling directional charge injection at bilateral solid-liquid interfaces. As a result, two series-connected electric double-layer capacitors are formed, delivering stable DC output without external rectification. The optimized LC-TENG achieves a short-circuit current of 100 μA, an open-circuit voltage of 684 V and a power density of 8.23 $W \cdot m^{-2}$, substantially outperforming conventional solid-liquid TENG devices. Benefiting from liquid self-lubrication and hermetic encapsulation, the device exhibits excellent operational stability under repeated mechanical bending and extended service conditions. This work proposes a novel triboelectric-liquid capacitance coupling mechanism that paves the way for high-performance, flexible micropower devices for self-powered wearable and IoT applications.

1. Introduction

The rapid proliferation of flexible wearable electronics and the Internet of Things (IoT) calls for miniaturized power sources that are mechanically flexible, maintenance-free, high in power density, and capable of direct current (DC) output [1–4]. Triboelectric nanogenerators (TENGs), which harvest ambient mechanical energy, have emerged as a promising candidate for powering such portable and flexible systems [5–7]. To enhance output performance and mechanical durability, TENG architectures have evolved from conventional solid-solid contact modes toward solid-liquid interfacial designs [8,9]. Yet traditional solid-solid TENGs suffer from two intrinsic drawbacks. One is severe mechanical wear that leads to structural failure under cyclic operation [10]. The other is an inherent alternating current (AC) output that demands additional rectification circuits, incurring extra energy loss and system bulk. Solid-liquid contact TENGs were developed to address these issues. The liquid medium reduces interfacial friction and wear, while the dynamic formation and relaxation of electric double layers (EDLs) at the solid-liquid interface enables intrinsic DC output, thereby eliminating the need for external rectification [11–15].

Water, as an efficient ionic conductor, ensures uniform contact and directional ion migration, thus sustaining continuous charge separation and stable DC generation [16–18]. Despite these advantages, state-of-the-art solid-liquid TENGs are not yet practical for real-world deployment. Three critical bottlenecks persist. First, most reported devices adopt open structures that resist hermetic encapsulation, resulting in poor long-term stability. Second, the single charge transport pathway limits further power density gains. Third, and most importantly, the EDL at conventional solid-liquid interfaces is highly susceptible to electrostatic shielding, which hinders efficient charge extraction and sustainable output [19–24]. These unresolved issues collectively impede the development of high-performance, robust, and flexible DC TENGs for

* Corresponding author at: Yunnan Normal University, School of Energy and Environment Science, Southwest United Graduate School, No.298, Yieryi Street, Kunming, Yunnan, 650092, China.
E-mail address: pzhyang@hotmail.com (P.-Z. Yang).
[1] These authors contributed equally.

https://doi.org/10.1016/j.cej.2026.179304
Received 3 June 2026; Accepted 8 July 2026
Available online 15 July 2026
1385-8947/© 2026 Elsevier B.V. All rights are reserved, including those for text and data mining, AI training, and similar technologies.

wearable and IoT applications.

Here, we propose a different paradigm for efficient DC generation based on triboelectric liquid capacitance coupling. Instead of a conventional binary solid-liquid configuration, we construct a solid-liquid-air triple-phase interface as the core working unit based on a porous polytetrafluoroethylene/carbon black heterostructure. This structure converts mechanical excitation into an asymmetric charge pump that directionally injects charges toward bilateral solid-liquid interfaces, inducing two series-connected EDL capacitors in situ. This design suppresses electrostatic shielding, enables synergistic ion electron transport for intrinsic DC output, and eliminates mechanical wear through self-lubrication and hermetic encapsulation. The resulting LC TENG delivers a short circuit current of 100 μA, an open circuit voltage of 684 V, and a peak power density of 8.23 $W{\cdot}m^{-2}$, outperforming traditional solid-liquid TENG devices TENGs, and shows negligible output degradation after repeated bending and long term operation.

2. Experimental section

2.1. Preparation of CB dispersion

Carbon black (CB) powder (commercial grade, average particle size ~30 nm, specific surface area ~ 120 $m^2{\cdot}g^{-1}$) was obtained from a commercial supplier in China. First, CB powder was mixed with anhydrous ethanol at a mass ratio of 1:50. The mixture was then stirred for 5 min using a vortex mixer to achieve preliminary dispersion. Finally, it was subjected to ultrasonic treatment for 10 min to ensure that the CB particles were fully and evenly dispersed, obtaining a uniform CB dispersion.

2.2. Preparation of TENG

Preparation of the p-PTFE layer/CB layer: Three p-PTFE samples, labeled as 01, 02 and 03, were used as flexible substrates. After plasma treatment (70 W, 180 s, O_2 atmosphere), the membranes were immersed in the as-prepared CB solution with their front surfaces fully submerged. The samples were then removed and blade-coated to form the embedded layer. Subsequently, the samples were flipped to their back sides (effective area, 4 cm × 3 cm) and attached with conductive silver cloth as the bottom electrode (positive output terminal). Conductive silver cloth (30 mm × 3 mm) was adhered to the upper surface of the p-PTFE/CB heterostructure as the top electrode (negative output terminal). Finally, polytetrafluoroethylene films with thicknesses of 0.05, 0.1 and 0.15 mm were used as encapsulation layers to prepare p-PTFE films of different thicknesses. Then, the positive and negative output terminals of the corresponding devices were connected to form a TENG, which was connected to a load to form a circuit for electrical performance testing.

2.3. Measurements and characterizations

Scanning electron microscopy (SEM) tests were conducted using a Thermo Quattro S system. Energy dispersive X-ray spectroscopy (EDS) tests were performed using an EDAX Octane Plus system. Contact angle tests were carried out using a JY-82B Kruss DSA system. X-ray photoelectron spectroscopy (XPS) tests were conducted using a Thermo Fisher Scientific K-Alpha system. The optical microscope used was the TDH series probe station, equipped with a stereo microscope. The open-circuit voltage (V_{OC}), short-circuit current (I_{SC}), and transferred charge (Q_{SC}) of the TENG were characterized using an electrometer (Keithley 6514) and an electrochemical workstation. Out-of-range voltages were measured using a 1000:1 high-voltage attenuation probe (100 MΩ input impedance) connected to the Keithley 6514 electrometer. The raw readings were multiplied by a factor of 1000 to obtain the actual voltage values. The Kelvin probe used for work function characterization was provided by KP Technology Ltd. (KP, USA). KPFM measurements were calibrated using a freshly sputtered gold (Au) standard sample with a known work function of 5.1 eV before each experiment to obtain absolute work function values. The contact force was monitored in real-time using a thin-film pressure sensor (CZ321) and maintained at 8 N and 50 N, respectively. The human wearable experiments were approved by the Ethics Committee of the School of Energy and Environmental Sciences (approval No. 1), and all participants provided written informed consent.

3. Results and discussion

3.1. Construction of efficient TENG

The core component of the LC-TENG is a porous polytetrafluoroethylene/carbon black (p-PTFE/CB) heterostructure. As shown in Fig. 1a, the device features a layered architecture [25] composed of a flat PTFE encapsulation film, a deionized water layer, a p-PTFE/CB composite with the CB side facing upward, and a bottom silver electrode adhered to the rear surface of the porous PTFE membrane. A narrow silver strip (30 mm × 3 mm) attached on the edge of the CB layer acts as the top electrode, leaving 92.5% of the CB surface exposed for direct water contact. Together, the deionized water layer and the p-PTFE/CB heterostructure form a stable solid-liquid-air triple-phase interface within the device [26]. During fabrication, the p-PTFE membrane is plasma-treated to reduce surface tension and improve the wettability of the CB dispersion. Coating the CB solution onto the plasma-activated PTFE surface produces a well-defined heterostructure with a continuous conductive CB top layer and a porous PTFE substrate (Fig. S1). Unlike conventional solid-solid and single-layer solid-liquid TENG configurations (Fig. S2), this structural design induces unique interfacial charge behavior and boosts the electrical output. The working principle of the LC-TENG can be understood using the equivalent circuit model in Fig. S3. The solid-liquid interface between the upper PTFE film and water is capacitor C1, while the interface between water and the underlying p-PTFE/CB heterostructure corresponds to capacitor C2. Unlike traditional solid-solid TENGs that rely on air breakdown for charge transfer (Fig. S4a), the dual-electrode LC-TENG creates efficient charge transport pathways at the triple-phase interface [27], enabling effective charge separation and transfer (Fig. S4b) [28].

Fig. 1b illustrates the working mechanism of the LC-TENG, which has three sequential stages. In the initial resting state, the bottom porous PTFE membrane is strongly electronegative and accumulates net negative charges from ambient air friction. At the same time, the intermediate CB layer interacts with the water film adsorbed at the solid-liquid interface. With its large specific surface area and abundant functional groups, the CB layer facilitates efficient interfacial charge transfer, forming a stable electric double layer (EDL_1) at the CB-water interface. At this stage, no ion migration pathway exists between the CB and PTFE layers, so the system is electrostatically balanced with no current output in the external circuit. In the contact stage, the upper hydrophobic PTFE film moves downward to contact the intermediate water layer, forming a second solid-liquid interface, the PTFE-water interface (EDL_2). Owing to the strong electronegativity and hydrophobicity of PTFE, this interface repels water molecules and traps negative triboelectric charges, inducing an enrichment of positive charges on the water side. The charge distribution of EDL_1 is dominated by the electrochemical properties of CB, whereas that of EDL_2 comes from the triboelectric characteristics of PTFE. The different charge-regulation mechanisms of the two interfaces create a potential asymmetry and an ion concentration gradient, which drives directional ion migration to compensate for the potential difference. In the charge redistribution stage, the upward separation of the top PTFE film from the water layer disrupts EDL_2 and eliminates the positive charge shielding layer on the water side. The excess positive ions previously accumulated around EDL_1 are released and diffuse freely into the bulk water through ion relaxation, allowing EDL_1 to recover to its initial state. This process weakens the positive charge layer on the water side of EDL_1 and changes the overall potential

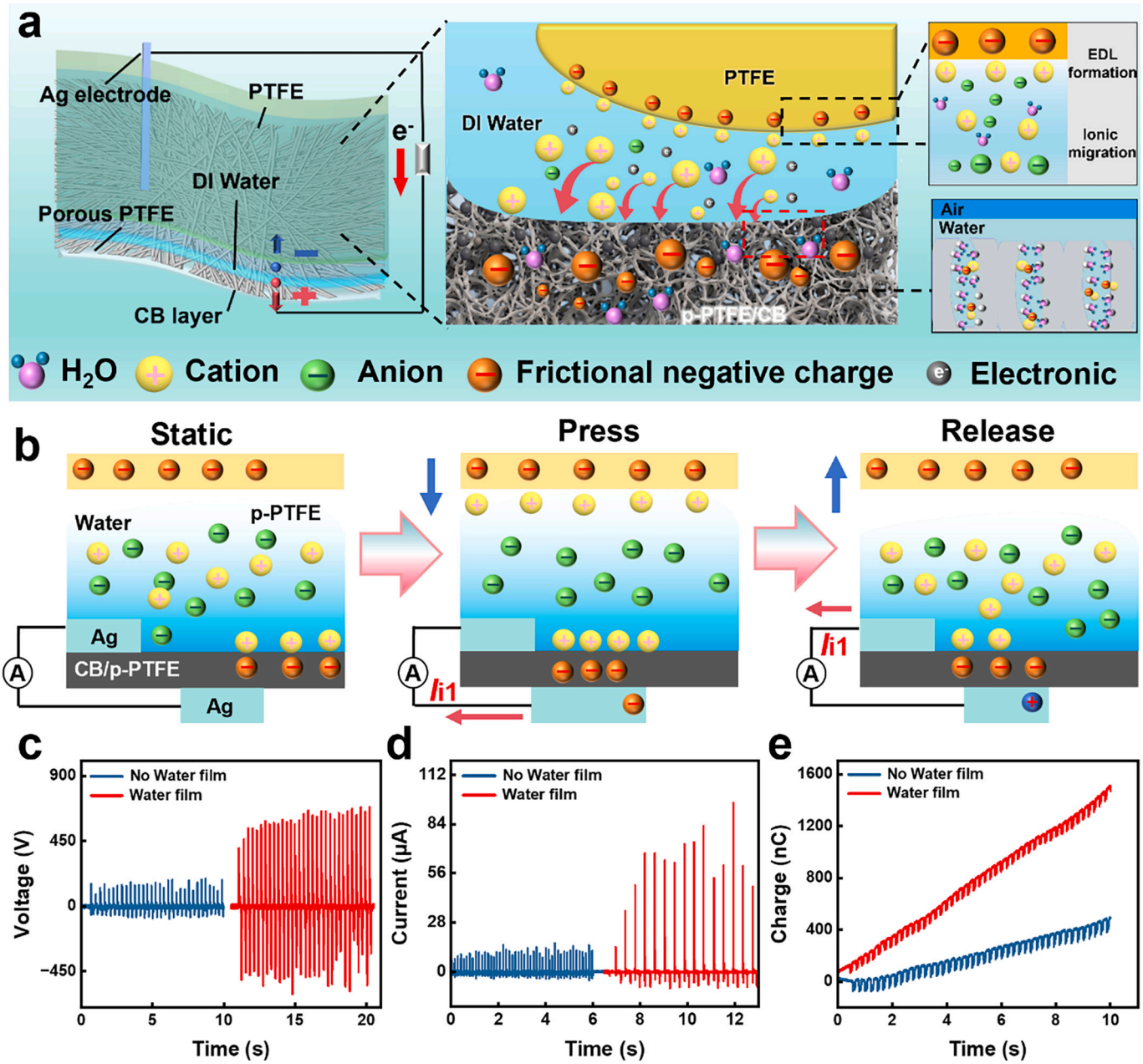

Fig. 1. Construction of High-Performance TENG. (a) Schematic diagram of the LC-TENG structure and charge transfer mechanism. (b) Schematic diagram of the working mode of LC-TENG. (c–e) V_{OC}, I_{SC}, and Q_{SC} of the LC-TENG with and without deionized water.

of the interfacial electrical bridge (Fig. S5) [29,30]. To clarify the contribution of the triple-phase interface to energy harvesting, we compared the electrical output of the LC-TENG with and without deionized water under identical mechanical excitation. Adding deionized water boosts the device performance. The open-circuit voltage rises from 194 V to 684 V (Fig. 1c), the short-circuit current increases from below 10 μA to 96 μA (Fig. 1d) and the transferred charge accumulated within 10 s increases from 495 nC to 1510 nC (Fig. 1e). Additional characteristic parameters confirm this consistent performance enhancement (Fig. S6). Deionized water thus acts not merely as a wetting medium but as an indispensable component that enables high-capacitance electric double-layer formation, promotes efficient ion transport, and guarantees DC output. This performance enhancement can be interpreted with the equivalent circuit model. The LC-TENG is a triboelectric charge-coupled power generation system whose open-circuit voltage is $V_{oc} = Q_{tribo} / (C_{eff} + C_p)$, where Q_{tribo} is the triboelectrically transferred charge, C_{eff} is the equivalent capacitance of the two series-connected electric double layers at the PTFE water and CB water interfaces, and C_p is the parasitic capacitance. Adding deionized water changes two key parameters. First, the liquid layer optimizes solid liquid interfacial contact, increasing Q_{tribo} by a factor of about 3.05. Second, the C_{eff} from the EDLs replaces the large air-gap parasitic capacitance C_p in dry devices. The overall system capacitance decreases by 13.6%. The increase in triboelectric charge and the decrease in total capacitance together elevate the output voltage by a factor of 3.53, matching the experimental results. Thus, the water medium serves two functions. It acts as a liquid capacitive layer for EDL construction and as a medium that promotes triboelectric charge transfer. The dual-electrode polarity output configuration delivers a current enhancement of two orders of magnitude compared with the single-electrode non-polarity mode. In the non-polarity mode, the bottom electrode is connected directly to a 1 MΩ load and produces a current of 0.8879 μA

(Fig. S7). A comparison with state-of-the-art liquid-based TENGs (Table S1) shows that our LC-TENG outperforms previous work.

3.2. Characterization and performance verification of the LC-TENG

In the initial state, the device presents a typical non-wetting solid-liquid-air triple-phase coexisting structure (Fig. S8) [31,32]. This interfacial architecture serves as an effective reservoir and modulation platform for ions and electrons. Upon external pressure loading, deionized water gradually permeates into the porous PTFE membrane driven by capillary force, constructing a well-distributed continuous triple-phase interface (Fig. S9). This stable interfacial configuration lays a solid physical foundation for subsequent charge exchange. The microstructural characteristics of the porous PTFE membrane determine the formation quality of the triple-phase interface. Three membranes with distinct pore structures, denoted as samples 01, 02, and 03, were chosen for comparative investigation. Fig. 2a and b display the SEM morphologies of the optimized sample 02 before and after modification. The pristine sample 02 has homogeneous fibrous networks with moderate pore size. After plasma treatment and carbon black deposition, CB nanoparticles are evenly anchored onto PTFE fiber skeletons, establishing interconnected conductive networks. For the untreated samples, sample 01 features the smallest pore size and densest fiber arrangement, sample 02 has a medium pore structure, and sample 03 exhibits the largest pores and loosest fibrous stacking. These morphological differences lead to distinct capillary force behaviors. The tiny pores of sample 01 generate high air gap resistance, hindering liquid infiltration. By contrast, samples 02 and 03, with larger pores, more easily form an intact triple-phase interface under mechanical compression (Fig. S10). Energy-dispersive X-ray spectroscopy results (Fig. S11) demonstrate that fluorine is concentrated along the fibrous frameworks, whereas carbon uniformly covers the fiber surfaces and inner pores. This spatially complementary elemental distribution verifies homogeneous and successful CB modification. The resulting composite structure integrates intact electron transport channels, and the interfacial bonding between CB and PTFE further enhances charge capture capability. Benefiting from the largest pore volume, sample 03 facilitates the construction of three-dimensional conductive pathways, which is favorable for charge extraction kinetics. However, as discussed below, its large pore size compromises wetting stability and interfacial charge retention, making sample 02 the optimal choice for the device substrate. Wettability is another critical parameter governing the formation of a stable triple-phase interface. All three untreated membranes exhibit inherent hydrophobicity, with contact angles larger than 90° in the absence of external compression. When mechanical pressure is applied, water progressively penetrates the porous channels and reduces the surface contact angle.

The extent of this reduction depends strongly on the membrane microstructure. Fully infiltrated sample 02 delivers a contact angle below 60° (Fig. 2c and d), demonstrating hydrophilicity and favorable liquid spreading capability. In comparison, samples 01 and 03 show only marginal decreases in contact angle and exhibit inferior wetting behavior (Figs. S12 and S13). Sample 02 is therefore selected as the optimal substrate. Its moderate pore size balances liquid permeability and interfacial structural stability. The excessively large pores in sample 03 trigger overly rapid water permeation, which impedes stable charge

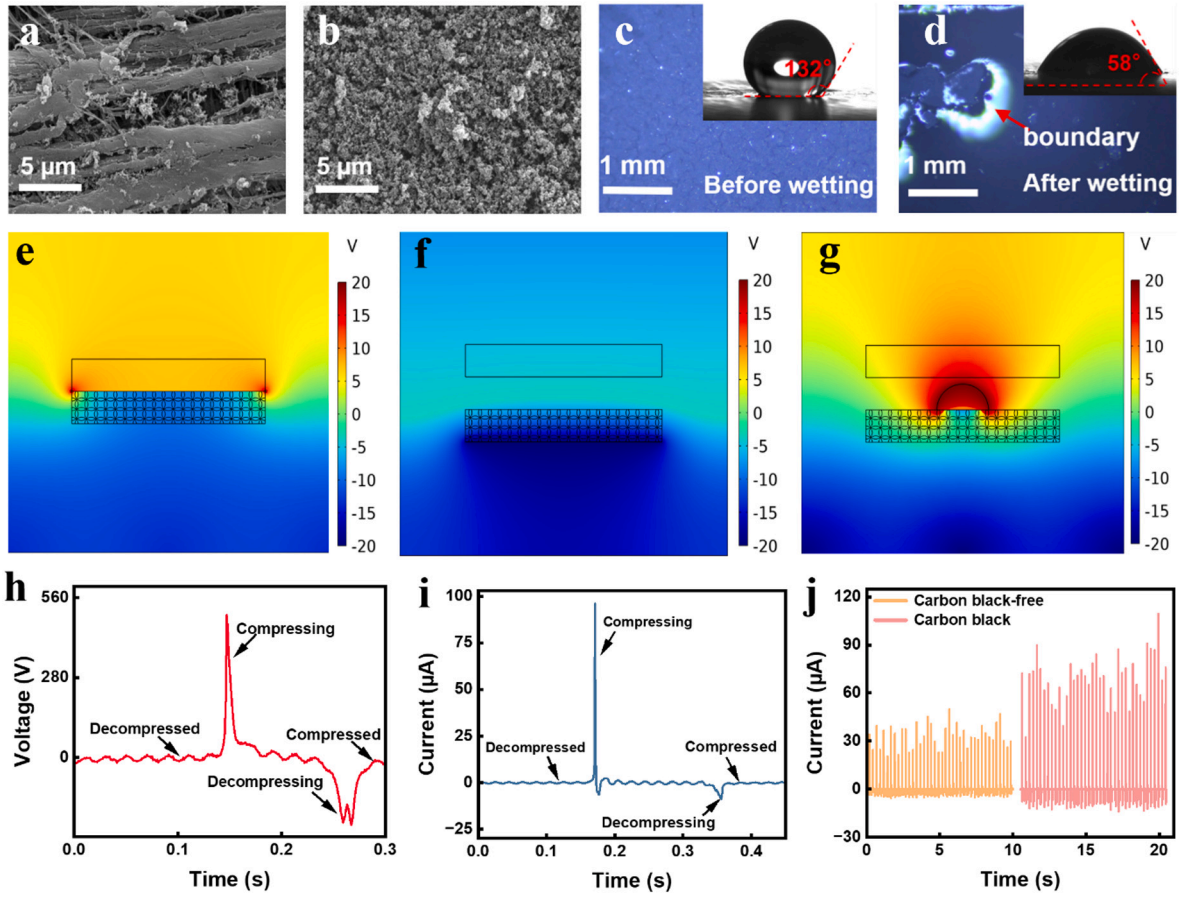

Fig. 2. Characterization and Performance Verification of the LC-TENG. (a–b) SEM images of the porous PTFE membrane before and after plasma treatment and CB coating. (c–d) Optical images and water contact angles of the porous PTFE membrane before and after wetting. (e–g) COMSOL electrostatic simulations of electric potential distribution under dry, fully water-filled, and triple-phase interface conditions. (h–i) Dynamic evolution of electrical signals of the device within a single operating cycle. (j) Comparison of short-circuit current with and without the carbon black layer.

separation and weakens interfacial charge accumulation. By contrast, the tiny pores of sample 01 severely restrict water infiltration, ultimately lowering energy conversion efficiency. X-ray photoelectron spectroscopy results (Fig. S14) confirm that plasma treatment introduces abundant oxygen-containing functional groups, including C—O and O-C=O bonds, onto the PTFE surface. These active groups strengthen the interfacial interaction between the PTFE substrate and carbon black [33,34]. The resulting robust chemical bonding guarantees efficient charge migration. Together with the structurally stable triple-phase interface, these merits jointly establish the fundamental working conditions of the fabricated device.

COMSOL Multiphysics simulations were conducted to reveal the suppressing effect of the triple-phase interface on water-induced electrostatic shielding. Fig. 2e–g present electric potential profiles under three distinct scenarios: the dry condition without water coverage, the fully saturated state covered by a continuous water film, and the triple-phase configuration with encapsulated air bubbles. A moderate and homogeneous interfacial electric field distribution is observed in the dry device. In the fully water-saturated sample, the high dielectric constant of water induces prominent electrostatic shielding, which dramatically reduces the surface potential and induced charge density. By contrast, the embedded air bubbles in the triple-phase architecture break the continuous liquid shielding effect due to the low dielectric constant of air [35]. The substantial dielectric discrepancy between air and water gives rise to an abrupt variation in electric field boundary conditions. Electric field lines become intensely concentrated inside the air bubbles, which remarkably elevates the local electric field intensity and induced charge density. These simulation results theoretically confirm that a porous structure can retain a residual air phase to mitigate liquid electrostatic shielding, thereby substantially boosting the output performance of solid-liquid coupled triboelectric nanogenerators. Fig. 2h and i depict the open-circuit voltage and short-circuit current profiles within a full working cycle. Both signals display direct-current pulses that synchronously respond to the contact-separation mechanical motion. A prominent positive peak emerges during the contact process, while a weak reverse signal is detected in the separation period. Stepwise charge accumulation within 10 s is recorded in charge measurement tests (Fig. S15), confirming stable and sustainable energy conversion capability. Electrode polarity measurements further elucidate the functional role of the carbon black layer. A positive current output is obtained when the CB layer acts as the negative electrode and the bottom porous PTFE electrode serves as the positive pole. Reversing the electrode connection correspondingly flips the current direction (Fig. S16), verifying the formation of an oriented charge transport pathway. The device output current declines sharply after the removal of the CB layer (Fig. 2j), demonstrating that the CB layer is indispensable for

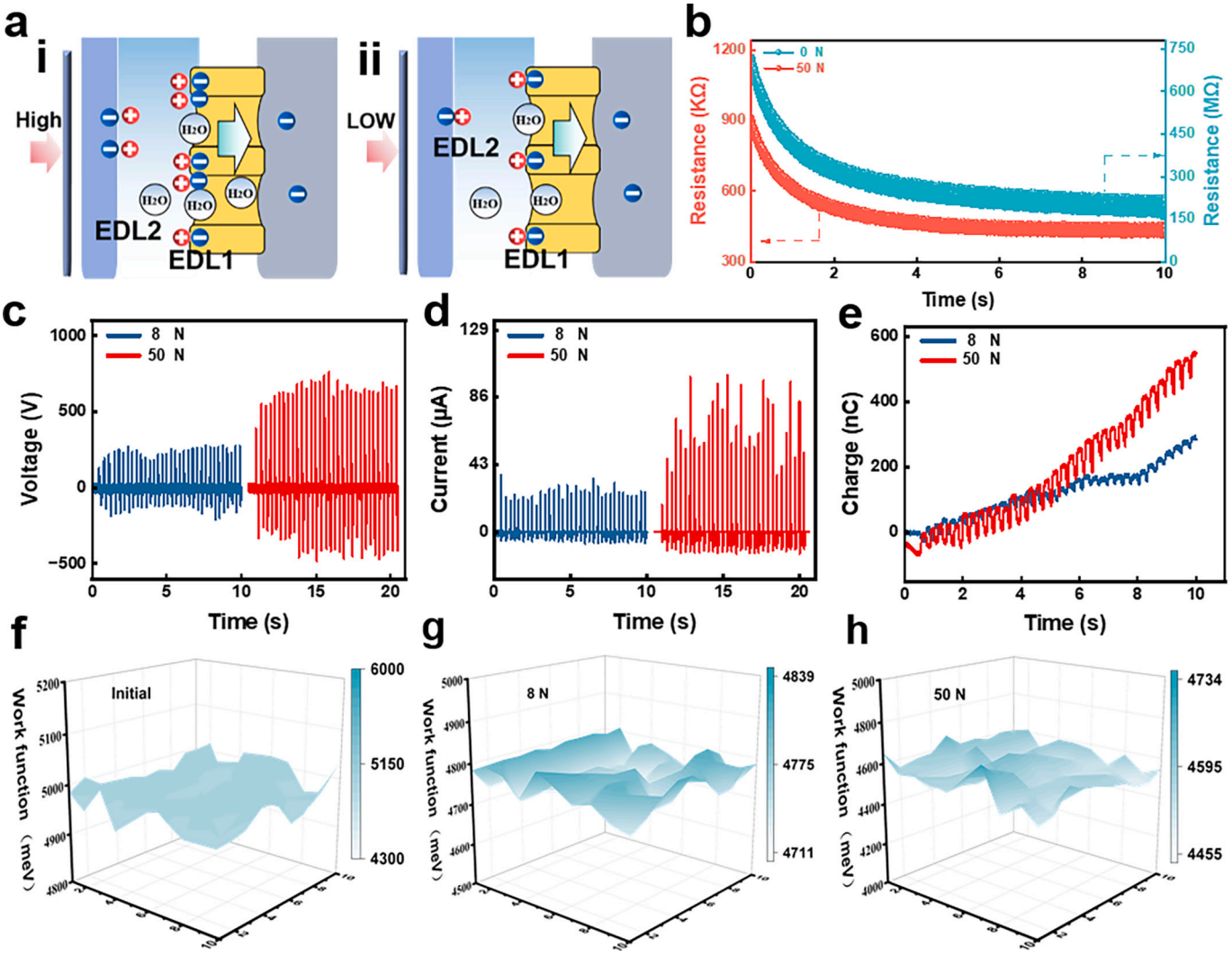

Fig. 3. The influence of contact pressure on the interfacial electrical transport characteristics of TENG. (a) Schematic diagram of contact under different pressure conditions. (b) Resistance curves of the LC-TENG under conditions with and without applied pressure. (c–e) V_{OC}, I_{SC}, and Q_{SC} of LC-TENG at different pressures. (f–h) Work function characterization diagrams of LC-TENG at rest, under 8 N contact, and under 50 N contact.

constructing an efficient ion-electron coupled interfacial system. Quantitative performance evaluation (Fig. S17) further validates this conclusion. Furthermore, electrostatic field modulation experiments (Fig. S18) further confirm that the device possesses tunable and controllable energy output capability, providing feasibility support for its application in intelligent sensing and self-powered systems.

3.3. The influence of contact pressure on the interfacial electrical transport characteristics of TENG

To explore charge transfer and energy conversion at the solid-liquid-air triple-phase interface, interfacial electrical transport was systematically investigated under varying contact pressure. Fig. 3a displays interfacial contact configurations under different mechanical loadings. Electrical characterization demonstrates that mechanical compression effectively optimizes interfacial contact quality. As shown in Fig. 3b, sharp declines in device resistance under applied pressure validate the improved efficiency of interfacial charge transport. Microscopic charge distribution evolution within the PTFE triboelectric layer across resting, contact, and separation states is visualized in Fig. S19. This visualization clarifies the dynamic process of charge redistribution and transport under variable mechanical pressure [36]. Device output performance was further evaluated under contact pressures of 8 N and 50 N (Fig. S20a–b). Open-circuit voltage, short-circuit current, and transferred charge increase steadily with elevated contact pressure in Fig. 3c–e. Enhanced mechanical driving strength facilitates interfacial charge generation and continuous charge transport [37]. These electrical results support the work function analysis that follows.

Kelvin probe force microscopy characterization reveals how mechanical pressure modulates interfacial polarization. The original work function of the CB-water composite film on the porous PTFE substrate is 4.976 eV (Fig. 3f). Slight mechanical contact reduces the work function to 4.764 eV (Fig. 3g), a decrease of 0.212 eV. Even a minor mechanical disturbance reorients water molecules at the interface. Further pressure increases drive the work function down to 4.563 eV (Fig. 3h).

The degree of interfacial polarization is thus positively correlated with external mechanical loading. Mechanical energy input promotes the directional alignment of water molecules at solid-liquid boundaries [38,39]. Fig. S21 compares devices constructed with different triboelectric materials to analyze how surface chemistry affects interfacial polarization. The initial work function of the CB-water film on the porous PTFE substrate is 5.053 eV. Surface coverage with a PTFE film reduces the work function to 4.449 eV. Additional coverage with a positively charged nylon film further lowers the work function to 4.331 eV (Table S3 and Fig. S22a–c). Materials with positive surface charges polarize interfacial water molecules more strongly. Parallel tests on conductive substrates confirm the universality of this polarization regulation. The work function of the pristine conductive substrate-water film is 4.928 eV. PTFE coverage lowers it to 4.445 eV, and nylon modification further reduces it to 4.361 eV. The same trend on both insulating and conductive substrates shows that electron affinity and electron-donating characteristics dominate water polarization (Table S4 and Fig. S23a–c). Electrode wetting also lowers the work function, from 4.526 eV to 4.232 eV (Fig. S24a and b), confirming that interfacial water polarization modulates surface electronic states. Interfacial water polarization and charge transfer are collectively regulated by external mechanical pressure and intrinsic material properties. Mechanical stimulation reorganizes interfacial water molecular orientation and accelerates charge generation and migration. Surface chemical characteristics of the triboelectric layer modulate interfacial electron transport, which in turn adjusts polarization intensity and charge extraction efficiency [40]. This dual modulation mechanism advances the fundamental understanding of triboelectric energy conversion and provides interfacial engineering strategies for designing high-performance self-powered devices.

3.4. Output optimization and application potential of TENG

Guided by the working mechanism, systematic investigations reveal the influence of core structural parameters and operating conditions on the output performance of the solid-liquid-air triple-phase interface direct current generator. Multi-mode output behaviors and environmental tolerance are further evaluated to assess the practical application potential of the device. Core structural parameters were optimized first. Fig. 4a presents the current output of devices assembled with three types of p-PTFE membranes marked as 01, 02, and 03. Devices based on membrane 02 deliver the best electrical output under identical test conditions. The unique pore architecture and surface characteristics of membrane 02 provide favorable conditions for efficient interfacial charge transport. Output variation corresponding to different thicknesses of the PTFE encapsulation layer is summarized in Fig. 4b. Samples with a thickness of 0.1 mm exhibit the highest short-circuit current. This moderate thickness achieves a balance between sufficient ion migration pathways and reduced transmission resistance. On the basis of the optimized thickness, Fig. 4c explores the correlation between effective device area and output capability. The device with an effective area of 4 $\times$ 4 cm^2 achieves the best comprehensive performance. Size scaling induces a tradeoff between improved charge collection efficiency and suppressed edge interference. Dynamic operating parameters were subsequently investigated to explore operational stability. The tolerance of device output to variable water content was verified by adjusting the spraying frequency from one to five times (Figs. S25 and S26). Current and voltage signals remain stable across the entire test range, demonstrating excellent adaptability to minor water content variations. This stable output originates from the self-balancing capability of the triple-phase interface under suitable moisture conditions. Insufficient water fails to form complete and continuous interfacial structures, while excessive water causes over-wetting of the porous framework and weakens the interfacial potential gradient. Spraying frequencies from one to five times ensure uniform gas-liquid distribution and sustainable dynamic equilibrium inside the porous channels. Device practicability in diverse liquid environments is further validated in Figs. S27 and S28. The device produces stable and repeatable electrical signals in various liquid media, including high-ionic-strength sodium chloride solution, low-polarity ethanol, deionized water, and tap water.

This broad environmental adaptability derives from the ability of different liquids to form stable interfacial electric double layers with solid substrates. Ionic liquids accelerate interfacial ion migration to strengthen electrical output, while nonpolar liquids participate in charge separation through molecular polarization. Both scenarios demonstrate the universality of the proposed triboelectric-liquid capacitance coupling mechanism [41,42]. Chemical environmental tolerance was further evaluated by testing device performance under different pH conditions. The system maintains stable output across a pH range from 1 to 12 (Figs. S29 and S30). Variations in H^+ and OH^- concentration have negligible influence on interfacial charge transfer. Device output is predominantly determined by the inherent contact charging properties of the functional materials and their interfacial double layer formation capability. Such characteristics guarantee reliable operation of the LC-TENG in chemically complex and variable working environments. Charge transport pathways were further optimized to boost the overall output capacity. Electrode connection configurations were systematically adjusted (Figs. S31 and S32). The optimal configuration connects one electrode to the rear side of the PTFE membrane and places the other electrode on the top CB layer. This structural design reduces parasitic capacitance between the two electrodes and builds an efficient charge extraction pathway throughout the triple-phase interfacial system. Devices fabricated under these optimized conditions deliver a stable output current of 100.4 μA and an open-circuit voltage of 657 V (Fig. 4d). This performance enhancement confirms that parasitic capacitance suppression amplifies the output. It also provides experimental evidence for the coupling mechanism

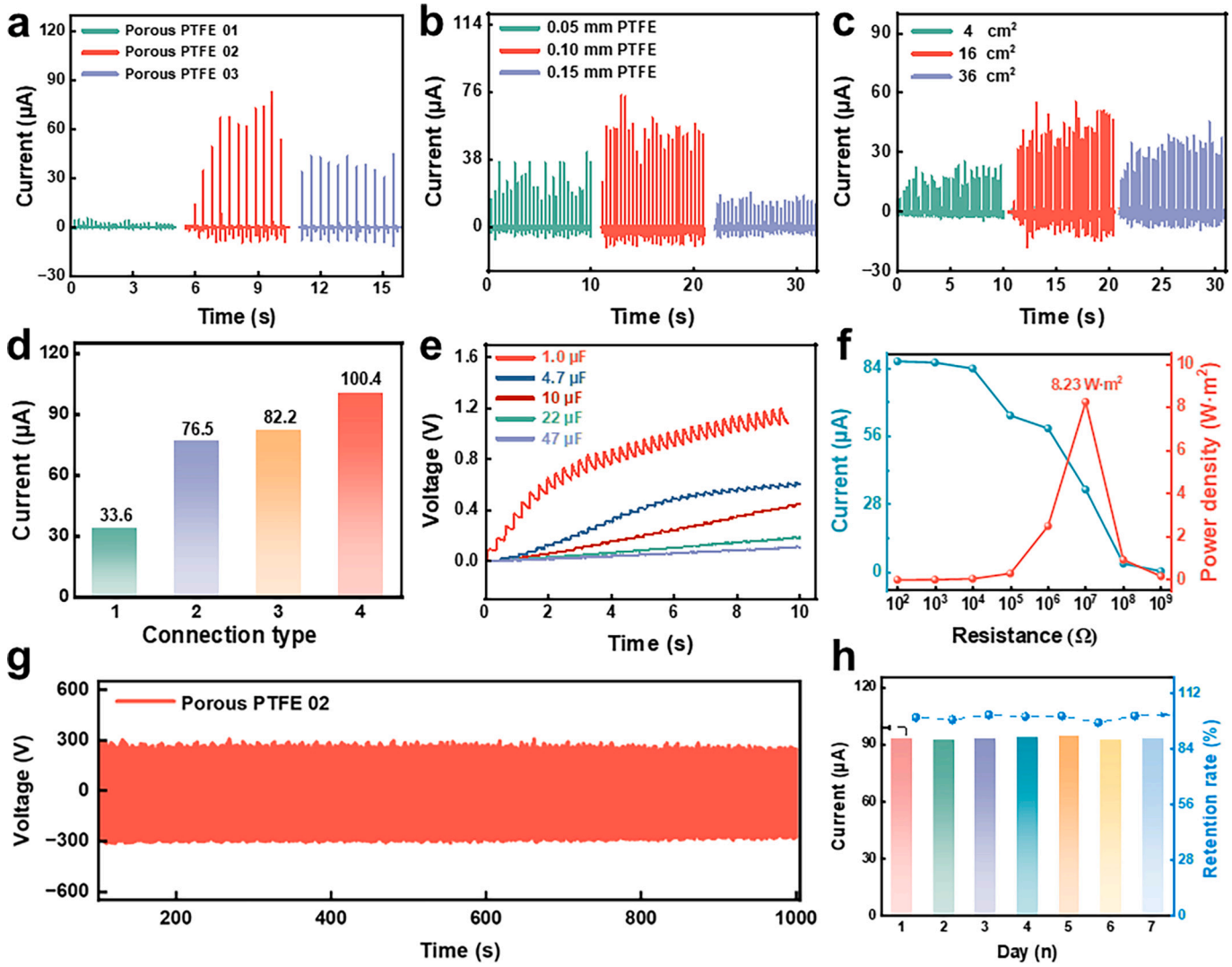

Fig. 4. Output Optimization and Application Potential of TENG. (a) I_{SC} of LC-TENGs composed of different porous PTFE membranes. (b) I_{SC} of LC-TENGs composed of different PTFE membranes. (c) I_{SC} of LC-TENGs with different areas of p-PTFE/CB heterostructure. (d) I_{SC} of LC-TENGs with different connection electrodes. (e) Charging capacity of the device at different capacitances. (f) Current-power curve of the device. (g) V_{OC} of LC-TENG after continuous operation for 1000 cycles. (h) I_{SC} of LC-TENG over seven days.

between triboelectric charge pumping and liquid capacitance behavior.

Benefiting from comprehensive structural and parametric optimization, the fabricated device exhibits application potential for micro-energy supply scenarios. The optimized device continuously powers various microelectronic components (Fig. 4e). The power density characterization in Fig. 4f gives a maximum of 8.23 $W{\cdot}m^{-2}$ based on a standard effective device area of 12 cm^2. This performance level enables reliable driving of diverse miniature electronic devices. Long-term operational and mechanical reliability were validated through repeated durability tests. The open-circuit voltage remains stable after 1000 continuous working cycles (Fig. 4g). No obvious performance degradation occurs after 600 bending-stretching cycles and one week of uninterrupted operation (Figs. 4h and S33 and S34). These results confirm the structural stability of the triple-phase interface and sustainable charge transfer efficiency under cyclic mechanical deformation and long-duration operation. This reliability supports the practical deployment of the device in flexible electronic systems. Optimization of structural geometry and operating parameters enhances the comprehensive performance of the direct-current triboelectric generator. The device features multi-scenario adaptability, favorable environmental tolerance, and outstanding long-term working stability. These merits enable sustainable mechanical energy harvesting and reliable self-powered system operation, giving the device broad application prospects in flexible wearable electronics. Future work will focus on improving output performance under frequent bending to better meet the requirements of wearable electronic applications.

3.5. *Application verification and system integration of TENG*

A highly integrated intelligent wireless sensing system was built using the optimized device architecture and operational parameters. The system was evaluated for basic electrical response, wearable adaptability, and overall integration performance. Fundamental output properties under mechanical excitation were examined first. Fig. 5a illustrates the correlation between applied pressure and output current. Current rises steadily with increased loading, reflecting good pressure sensitivity. Fig. 5b presents output voltage recorded at different working frequencies. Stable electrical signals are maintained over a broad frequency range. This feature guarantees reliable operation as a self-powered sensor under diverse mechanical conditions [43]. Fig. 5c compares current signals collected from typical human movements such as finger tapping and palm slapping. Distinct pulse waveforms

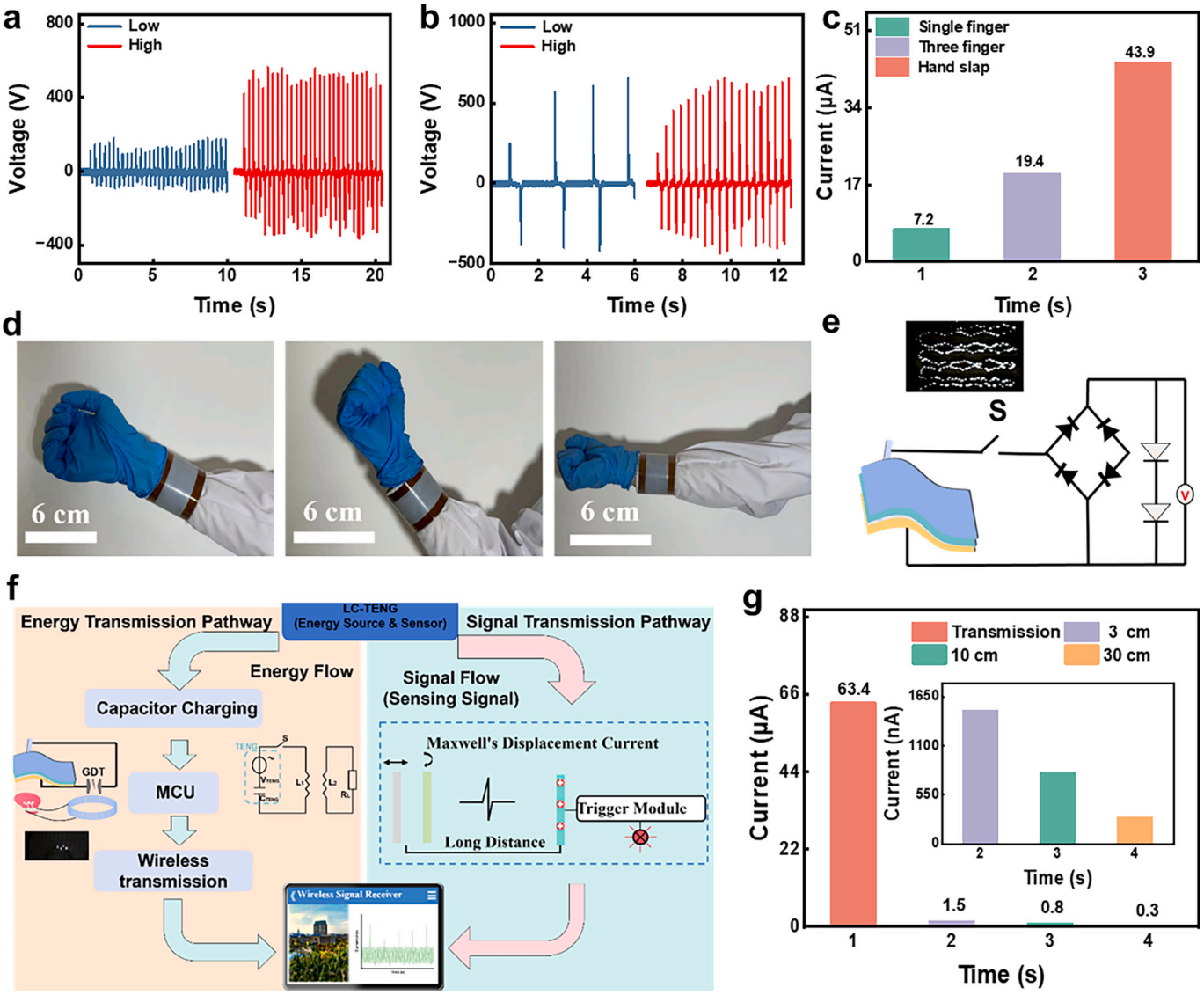

Fig. 5. Application Verification and System Integration of TENG. (a) Pressure response characteristics of LC-TENG. (b) *Voc* of LC-TENG at different frequencies. (c) I_{SC} under different tapping methods. (d) Photo of flexible LC-TENG seamlessly integrated with clothing. (e) Equivalent circuit and physical picture of LC-TENG in series with a light bulb. (f) Workflow diagram of the wireless sensing system. (g) Current response at transmission distances of 3 cm, 10 cm and 30 cm.

correspond to different motion patterns, and the device can harvest mechanical energy from daily human activities.

Wearable application performance was tested next. The ultrathin and flexible device fits closely onto human skin or fabric substrates (Fig. 5d). Steady voltage output is sustained during arm swinging and foot stepping (Fig. S35). A commercial LED array was used to verify practical power supply capacity. The device lights up 235 LED units independently with no external power supply (Fig. 5e). A full-scale wireless sensing system was constructed to assess system-level compatibility. Fig. 5f outlines the overall framework consisting of three functional units. One unit handles mechanical energy collection and power regulation. Another undertakes signal capture and feature analysis. The last unit realizes remote data transmission via wireless communication technology [44,45]. Wireless signal transmission tests were conducted at working distances of 3 cm, 10 cm, and 30 cm. Fig. 5g summarizes the received current at different distances. Current magnitude declines gradually as transmission distance grows due to reduced spatial coupling efficiency [46–48]. Detectable signals are still captured at 30 cm. This performance meets the basic requirements for near-field data exchange between wearable hardware and portable terminals. Combined results from device optimization and system integration demonstrate the application potential of the proposed direct-current generator in wearable electronics, the Internet of Things, and intelligent sensing. This study also provides solid technical support for the development of advanced self-powered electronic systems.

4. Conclusion

This work establishes a triboelectric-liquid capacitance coupling paradigm for direct-current energy harvesting. The solid-liquid-air triple-phase interface alleviates electrostatic shielding and improves interfacial charge transport. The porous heterostructure generates a charge pump effect that connects two interfacial electric double layers in series and enables coupled ion-electron transport. This mechanism allows the solid-liquid system to produce steady direct-current output without external rectification. The optimized LC-TENG gives a short-circuit current of 100 μA, an open-circuit voltage of 684 V, and a peak power density of 8.23 $W{\cdot}m^{-2}$. These values exceed those of most previously reported solid-liquid triboelectric nanogenerators. Long-term cycling tests confirm stable operation with negligible charge leakage

and performance loss. This work reveals how triple-phase interface engineering regulates electrostatic shielding and facilitates charge migration. It provides a practical strategy for designing high-performance flexible direct-current micro-power devices for wearable and intelligent electronics.

CRediT authorship contribution statement

Xin-Long Xiao: Writing – review & editing, Writing – original draft. **Jiang-Tao Guo:** Methodology, Writing – review & editing. **Sheng-Jie Lin:** Data curation, Investigation. **Wen Yang:** Formal analysis, Validation. **Yun-Bo Zhang:** Formal analysis, Software. **Yong Zhang:** Data curation, Visualization. **Pei-Zhi Yang:** Writing – review & editing, Funding acquisition, Supervision.

Declaration of competing interest

The authors declare that they have no known competing financial interests or personal relationships that could have appeared to influence the work reported in this paper.

Acknowledgment

This work was supported by Yunnan Provincial Science and Technology Project at Southwest United Graduate School (Grant No. 202302A0370009), National Natural Science Foundation of China (No. U1802257), Yunnan Revitalization Talent Support Program, the Spring City Plan: The High-level Talent Promotion and Training Project of Kunming (2022SCP005), Project for Building a Science and Technology Innovation Center Facing South Asia and Southeast Asia (202403AP140015).

Appendix A. Supplementary data

Supplementary data to this article can be found online at https://doi.org/10.1016/j.cej.2026.179304.

Data availability

Data will be made available on request.

References

[1] J. Guo, L. Duan, W. Yang, Q. Wang, Y. Zhang, Y. Zhang, Z.L. Wang, P. Yang, Multiphase soft metal enabled high-performance fabric-based wearable energy harvesting, Nano Energy 131 (2024) 110305, https://doi.org/10.1016/j.nanoen.2024.110305.

[2] L. Xia, H. Zhou, J. Chen, F. Liu, S. Chang, Y. Huang, J. Jiang, K. Dong, Y. Wu, C. Zhang, Human body electrode enabled direct current triboelectric nanogenerator for self-powered wireless human motion and environment monitoring, Adv. Electron. Mater. 10 (6) (2024) 2300713, https://doi.org/10.1002/aelm.202300713.

[3] J. Fan, C. Lou, P. Cui, Q. Xia, L. Wang, Y. Chang, A. Zhou, A wearable self-charging power system integrating micro-supercapacitors and triboelectric nanogenerators with MXene-coated fabric as conductive layer, Adv. Powder Mater. (2025) 100341, https://doi.org/10.1016/j.apmate.2025.100341.

[4] Y. Zhang, E. Wang, H. Ouyang, Z. Li, Self-powered wearable sensing devices for digital health, Mater. Horiz. 12 (17) (2025) 6681–6706, https://doi.org/10.1039/D5MH00443H.

[5] Y. Lee, S. Lim, W.J. Song, S. Lee, S.J. Yoon, J.M. Park, M.G. Lee, Y.L. Park, J.Y. Sun, Triboresistive touch sensing: grid-free touch-point recognition based on monolayered ionic power generators, Adv. Mater. 34 (19) (2022) 2108586, https://doi.org/10.1002/adma.202108586.

[6] Y. Xu, Z. Sun, Z. Bai, H. Shen, R. Wen, F. Wang, G. Xu, C. Lee, Bionic e-skin with precise multi-directional droplet sliding sensing for enhanced robotic perception, Nat. Commun. 15 (1) (2024) 6022, https://doi.org/10.1038/s41467-024-50270-8.

[7] S. Guo, Y. Zhang, Z. Yu, M. Dai, X. Liu, H. Wang, S. Liu, J.J. Koh, W. Sun, Y. Feng, Leaf-based energy harvesting and storage utilizing hygroscopic iron hydrogel for continuous power generation, Nat. Commun. 16 (1) (2025) 5267, https://doi.org/10.1038/s41467-025-60341-z.

[8] Y. Li, Y. Luo, H. Deng, S. Shi, S. Tian, H. Wu, J. Tang, C. Zhang, X. Zhang, J.W. Zha, Advanced dielectric materials for triboelectric nanogenerators: principles, methods, and applications, Adv. Mater. 36 (52) (2024) 2314380, https://doi.org/10.1002/adma.202314380.

[9] J. Zhu, M. Zhu, Q. Shi, F. Wen, L. Liu, B. Dong, A. Haroun, Y. Yang, P. Vachon, X. Guo, Progress in TENG technology—a journey from energy harvesting to nanoenergy and nanosystem, Ecomat 2 (4) (2020) e12058, https://doi.org/10.1002/eom2.12058.

[10] C. Pan, J. Meng, L. Jia, X. Pu, Droplet-based direct-current electricity generation induced by dynamic electric double layers, ACS Appl. Mater. Interfaces 16 (14) (2024) 17649–17656, https://doi.org/10.1021/acsami.4c01168.

[11] K. Cha, S. In, S.H. Chung, M. Jee, Y. Jin, J. Hong, S. Lee, Improving electrical performance and lifespan of liquid-based triboelectric nanogenerator via charge-inducing structure, Adv. Funct. Mater. 35 (41) (2025) 2505695, https://doi.org/10.1002/adfm.202505695.

[12] S. Qin, P. Yang, Z. Liu, J. Hu, N. Li, L. Ding, X. Chen, Triboelectric sensor with ultra-wide linear range based on water-containing elastomer and ion-rich interface, Nat. Commun. 15 (1) (2024) 10640, https://doi.org/10.1038/s41467-024-54980-x.

[13] S. Gong, K. Li, J. Sun, J. Chen, H. Guo, Interfacial droplet-based triboelectric nanogenerator with optimized architecture for highly efficient vibrational energy conversion, Joule 9 (1) (2025), https://doi.org/10.1016/j.joule.2024.09.010.

[14] J. Wang, P. Cui, J. Zhang, Y. Ge, H. Meng, C. Feng, H. Liu, L. Liu, J. Wang, N. Xuan, Boosted energy harvesting in droplet electrochemical cell with non-equilibrium electrical double layer, Nano Energy 112 (2023) 108437, https://doi.org/10.1016/j.nanoen.2023.108437.

[15] X. Chen, Y. Zhang, Y. Huang, Y. Zhao, F. Wang, P. Wu, Z.L. Wang, X. Mu, Y. Yang, Interfacial polarization-enhanced ultrahigh performance liquid droplet nanogenerator, Adv. Energy Mater. 15 (29) (2025) 2406116, https://doi.org/10.1002/aenm.202406116.

[16] J. Wang, H. Wu, S. Fu, G. Li, C. Shan, W. He, C. Hu, Enhancement of output charge density of TENG in high humidity by water molecules induced self-polarization effect on dielectric polymers, Nano Energy 104 (2022) 107916, https://doi.org/10.1016/j.nanoen.2022.107916.

[17] Q. Zhang, Y. Li, H. Cai, M. Yao, H. Zhang, L. Guo, Z. Lv, M. Li, X. Lu, C. Ren, A single-droplet electricity generator achieves an ultrahigh output over 100 V without pre-charging, Adv. Mater. 33 (51) (2021) 2105761, https://doi.org/10.1002/adma.202105761.

[18] C. Yang, Y. Wang, Y. Wang, Z. Wang, Y. Guo, L. Zhang, X. Liu, H. Chen, Skeleton enhanced dispersed lubricant particle based triboelectric nanogenerator for droplet energy harvesting, Adv. Sci. 12 (31) (2025) e05363, https://doi.org/10.1002/advs.202505363.

[19] C. Ye, D. Liu, Y. Gao, F. Liu, H. Xu, T. Jiang, Z.L. Wang, Electrostatic breakdown at liquid-solid-gas triple-phase interfaces owing to contact electrification, Matter 8 (4) (2025), https://doi.org/10.1016/j.matt.2025.102007.

[20] X. Li, S. Li, X. Guo, J. Shao, Z.L. Wang, D. Wei, Triboiontronics for efficient energy and information flow, Matter 6 (11) (2023) 3912–3926, https://doi.org/10.1016/j.matt.2023.08.022.

[21] X. Li, R. Li, S. Li, Z.L. Wang, D. Wei, Triboiontronics with temporal control of electrical double layer formation, Nat. Commun. 15 (1) (2024) 6182, https://doi.org/10.1038/s41467-024-50518-3.

[22] X. Li, Y. Wei, X. Gao, Z. Zhang, Z.L. Wang, D. Wei, Harnessing triboiontronic Maxwell's demon by triboelectric-induced polarization for efficient energy-information flow, Joule 9 (5) (2025), https://doi.org/10.1016/j.joule.2025.101888.

[23] Y. Liu, P. Peng, F. Yang, Z.L. Wang, D. Wei, Printable high-performance iontronic power source based on osmotic effects, Energy Mater. 5 (6) (2025), https://doi.org/10.20517/energymater.2024.187. N/A–N/A.

[24] S. Li, Z. Zhang, F. Yang, X. Li, P. Peng, Y. Du, Q. Zeng, M. Willatzen, Z.L. Wang, D. Wei, Transistor-like triboiontronics with record-high charge density for self-powered sensors and neurologic analogs, Device 2 (6) (2024), https://doi.org/10.1016/j.device.2024.100332.

[25] J. Nie, Z. Ren, L. Xu, S. Lin, F. Zhan, X. Chen, Z.L. Wang, Probing contact-electrification-induced electron and ion transfers at a liquid–solid interface, Adv. Mater. 32 (2) (2020) 1905696, https://doi.org/10.1002/adma.201905696.

[26] J. Guo, L. Duan, W. Yang, Q. Wang, X. Feng, Y. Zhang, Y. Zhang, Z.L. Wang, P. Yang, Flexible triboelectric nanogenerator arrays for energy harvesting and direct current output via solid-liquid-gas interfaces involving liquid metals, Adv. Funct. Mater. 35 (49) (2025) e10233, https://doi.org/10.1002/adfm.202510233.

[27] Y. Kang, H. Wu, H. Yi, J. Wang, S. Xu, K. Li, G. Li, Q. Zhao, X. Wang, C. Hu, Surface non-equilibrium state induced by unipolar charge collection for constructing constant current power generation, Adv. Funct. Mater. 35 (42) (2025) 2505503, https://doi.org/10.1002/adfm.202505503.

[28] C. Xu, J. Yu, Z. Huo, Y. Wang, Q. Sun, Z.L. Wang, Pursuing the tribovoltaic effect for direct-current triboelectric nanogenerators, Energ. Environ. Sci. 16 (3) (2023) 983–1006, https://doi.org/10.1039/D2EE04019K.

[29] C. Qin, D. Wang, Y. Liu, P. Yang, T. Xie, L. Huang, H. Zou, G. Li, Y. Wu, Tribo-electrochemistry induced artificial solid electrolyte interface by self-catalysis, Nat. Commun. 12 (1) (2021) 7184, https://doi.org/10.1038/s41467-021-27494-z.

[30] X. Zhang, D. Ren, H. Wu, J. Wang, X. Li, H. Yang, Q. Li, Q. Yang, J. Zhu, Y. Xi, Ultrahigh voltage direct current quasi-tribovoltaic nanogenerator by switchable tribo-bias induction and deposited charge extraction, Energ. Environ. Sci. 17 (12) (2024) 4175–4186, https://doi.org/10.1039/d4ee01067a.

[31] L. Liu, L. Lei, Contact angle on rough curved surfaces and its implications in porous media, Langmuir 39 (12) (2023) 4507–4517, https://doi.org/10.1021/acs.langmuir.3c00213.

[32] Z. Tang, D. Yang, H. Guo, S. Lin, Z.L. Wang, Spontaneous wetting induced by contact-electrification at liquid–solid interface, Adv. Mater. 36 (25) (2024) 2400451, https://doi.org/10.1002/adma.202400451.
[33] S.B. Ghode, C.S. Patil, J. Kim, V.P. Bhandigare, J. Kim, A. Mannan, Y. Ko, S.R. Patil, M. Noman, Q.M. Saqib, Plasma-assisted surface modification and formation of oxygen vacancies in coffee-derived carbon for triboelectric energy harvesting and electrocatalytic water splitting, Nano Energy 141 (2025) 111116, https://doi.org/10.1016/j.nanoen.2025.111116.
[34] X. Sun, Y. Liu, N. Luo, Y. Liu, Y. Feng, S. Chen, D. Wang, Controlling the triboelectric properties and tribological behavior of polyimide materials via plasma treatment, Nano Energy 102 (2022) 107691, https://doi.org/10.1016/j.nanoen.2022.107691.
[35] J. Chai, G. Wang, J. Zhao, G. Wang, C. Wei, A. Zhang, G. Zhao, Robust, breathable, and chemical-resistant polytetrafluoroethylene (PTFE) films achieved by novel in-situ fibrillation strategy for high-performance triboelectric nanogenerators, Nano Res. 17 (3) (2024) 1942–1951, https://doi.org/10.1007/s12274-023-6147-3.
[36] F. Zhan, A.C. Wang, L. Xu, S. Lin, J. Shao, X. Chen, Z.L. Wang, Electron transfer as a liquid droplet contacting a polymer surface, ACS Nano 14 (12) (2020) 17565–17573. https://pubs.acs.org/doi/10.1021/acsnano.0c08332.
[37] S. Li, S. Deng, R. Xu, D. Liu, Y. Nan, Z. Zhang, Y. Gao, H. Lv, M. Li, Q. Zhang, High-frequency mechanical energy harvester with direct current output from chemical potential difference, ACS Energy Lett. 7 (9) (2022) 3080–3086, https://doi.org/10.1021/acsenergylett.2c01582.
[38] Y. Jin, S. Yang, M. Sun, S. Gao, Y. Cheng, C. Wu, Z. Xu, Y. Guo, W. Xu, X. Gao, How liquids charge the superhydrophobic surfaces, Nat. Commun. 15 (1) (2024) 4762, https://doi.org/10.1038/s41467-024-49088-1.
[39] S. Lin, L. Zhu, Z. Tang, Z.L. Wang, Spin-selected electron transfer in liquid–solid contact electrification, Nat. Commun. 13 (1) (2022) 5230, https://doi.org/10.1038/s41467-022-32984-9.
[40] M. Yang, K. Xiong, X. Chen, H. Zhong, S. Lin, Ultra-low-power-consuming liquid-water-based optoelectronic computing chip, Device 2 (12) (2024), https://doi.org/10.1016/j.device.2024.100547.
[41] H. Qin, L. Xu, S. Lin, F. Zhan, K. Dong, K. Han, H. Wang, Y. Feng, Z.L. Wang, Underwater energy harvesting and sensing by sweeping out the charges in an electric double layer using an oil droplet, Adv. Funct. Mater. 32 (18) (2022) 2111662, https://doi.org/10.1002/adfm.202111662.
[42] H. Luo, X. Ni, Y. Cui, C. Huang, P. Yuan, T. Yang, J. Shao, X. Huang, High stability rotary solid-liquid triboelectric nanogenerator for ionic liquid detection, Nano Energy 138 (2025) 110870, https://doi.org/10.1016/j.nanoen.2025.110870.
[43] G. Zheng, C. Xing, L. Zhang, Y. Tan, M. Shan, Intelligent road driven by self-powered wireless sensors networks based on triboelectric nanogenerators: principles, applications, and perspectives, Measurement (2025) 118815, https://doi.org/10.1016/j.measurement.2025.118815.
[44] H. Sun, X. Li, Z. Zhao, X. Liu, X. Sun, Z. Li, W. Qiao, L. He, F. Yi, J.S. Zhao, Kirigami cube-inspired triboelectric vector sensor for human–machine interaction, Adv. Funct. Mater. 36 (11) (2026) e16876, https://doi.org/10.1002/adfm.202516876.
[45] S. Liu, S. An, X. Zhou, J. Wang, X. Pu, A self-powered, process-oriented wireless sensor with high discharge signal density, Device 2 (9) (2024), https://doi.org/10.1016/j.device.2024.100437.
[46] H. Hong, C. Yan, Y. Hu, J. Yang, B. Chen, L. Liu, Z. Wang, H. Wu, Achieving ultra-high-power output in triboelectric energy harvesters by torrent-like charge regulation, Adv. Mater. 37 (51) (2025) 2506136, https://doi.org/10.1002/adma.202506136.
[47] C. Li, S. Xu, E. Zhao, Y. Sun, T. Wang, G. Min, J. He, Z.L. Wang, W. Tang, Chip-less, self-powered electronic patch for wireless sensing and communication, Nat. Sens. 1 (2026) 270–278, https://doi.org/10.1038/s44460-026-00033-3.
[48] S. An, S. Liu, X. Zhou, G. Li, J. Wang, T. Zhou, A. Yang, Y. Zhou, X. Pu, Z.L. Wang, Self-powered triboelectric wireless sensor for robotic arm control via enhanced electromagnetic induction, Nat. Sens. (2026) 341–349, https://doi.org/10.1038/s44460-026-00039-x.